Highly efficient water oxidation via a bimolecular reaction mechanism on rutile structured mixed-metal oxyfluorides

Zahra Gohari-Bajestani, Xiao Wang, Amandine Guiet, Romain Moury, Jean-Marc Grenèche, Annie Hémon-Ribaud, Yuxuan Zhang, Daniel Chartrand, Vincent Maisonneuve, Ali Seifitokaldani, et al.

Version of Record: https://www.sciencedirect.com/science/article/pii/S2667109322001142
Manuscript_7f61eda89712c55f12b336167b220815

Highly efficient water oxidation via a bimolecular reaction mechanism on rutile structured mixed-metal oxyfluorides

Zahra Gohari-Bajestani,[1‡] Xiao Wang,[2‡] Amandine Guiet,[1] Romain Moury,[1] Jean-Marc Grenèche,[1] Annie Hémon-Ribaud,[1] Yuxuan Zhang,[3] Daniel Chartrand,[3] Vincent Maisonneuve,[1] Ali Seifitokaldani,[2*] Nikolay Kornienko,[3*] Jérôme Lhoste [1*]

[1]Institut des Molécules et Matériaux du Mans (IMMM), UMR 6283 CNRS, Le Mans Université, Avenue Olivier Messiaen, 72085 Le Mans Cedex 9, France

[2]Department of Chemical Engineering, McGill University, 3610 University Street, Montréal, Québec H3A 0C5, Canada

[3]Department of Chemistry, Université de Montréal, 1375 Ave. Thérèse-Lavoie-Roux, Montréal, Québec, H2V 0B3, Canada

[‡]Equal Contribution

*corresponding authors: jerome.lhoste@univ-lemans.fr, nikolay.kornienko@umontreal.ca, and ali.seifitokaldani@mcgill.ca

Lead contact: nikolay.kornienko@umontreal.ca

Summary

Mixed-metal oxides are generally considered to be the highest-performance catalysts for alkaline water oxidation. Despite significant efforts dedicated to understanding and accelerating their efficiency, most works have been limited investigations of Ni, Co, and Fe oxides, thus overlooking beneficial effects of hetero-anion incorporation. To this end, we report on the development of $Co_{0.5}Fe_{0.5}O_{0.5}F_{1.5}$ oxyfluoride catalyst with highly effective catalytic sites for electrochemical water oxidation. In particular, its performance across metrics of Tafel slope (27 mV/dec), mass activity (846 A/g at 1.53 V vs. RHE), turnover frequency (21/s at 1.53 V vs. RHE), overpotential (220 mV for 10 mA/cm^2), and stability (27 days of continuous operation) largely surpasses most known Co-based catalysts. Mechanistic studies suggest that this performance is driven by a bimolecular, oxygen coupling reaction mechanism through proximal active sites on the catalyst surface, thus enabling a new avenue for achieving accelerated oxygenic electrocatalysis.

Introduction

Impacts on global climate and environmental decay are increasingly evident as consequences of human activities[1]. Mitigating these effects will ultimately be underpinned by the transition to sustainable means of energy harvesting and consumption, within which electrochemical technologies stand to play a critical role[2-4]. Widespread adoption of electrochemical water and CO_2 reduction to form H_2 or C-based fuels is hampered by the kinetics of the oxygen evolution reaction (OER) and thus, much work in the field is dedicated towards OER catalyst discovery[5]. To this end, mixed-metal oxides have emerged as the top class of materials for this reaction in alkaline conditions[6]. The recent decade of work in the field has yielded important gains in understanding the roles of incorporating Fe impurities, lattice strain, substrate effects, interfaces and exfoliation[7-11]. In an orthogonal direction, the modification of the catalytically active sites through hetero-element incorporation has yielded substantial gains in performance over purely Ni/Co/Fe oxides, though most efforts focus on cationic incorporation[12]. In contrast, anionic incorporation is seldom used, largely due to synthetic challenges, especially in the direction of fluoride substitution. However, initial reports suggest that hetero-anionic compounds hold much promise as OER catalysts, though the factors driving these observations are not fully settled[13-19]. Often, metal oxides catalyze the OER through sequential proton-coupled electron transfer steps. This inevitably limits their performance via scaling relations as all intermediates share a M-O bond.[20] Breaking these scaling relations for enhanced OER performance can be accomplished by accessing new reaction mechanisms such as radical oxygen coupling and lattice oxygen involvement, and the discovery of new OER catalyst compositions ultimately underpins access to such reaction pathways.

Numerous synthetic routes have been used to prepare functional transition metal oxyfluorides to control the chemical composition with specific fluorination degree, particle size, morphology, and stabilization of desired crystal structures[21-25]. In this work, we report on the two-step preparation of a new cobalt iron oxyfluoride with a rutile type structure, $Co_{0.5}Fe_{0.5}O_{0.5}F_{1.5}$, obtained by calcination of the hydrated fluoride $CoFeF_5(H_2O)_7$. Subsequent electrocatalytic evaluations unveiled that $Co_{0.5}Fe_{0.5}O_{0.5}F_{1.5}$ is one of the highest performing cobalt-based OER catalysts reported to date, considering metrics of overpotential, Tafel slope, mass activity, and stability. Complementary lines of computational and mechanistic studies were carried out to elucidate that the existence of a bimolecular reaction mechanism that is deemed to be the origin of the high efficiency of $Co_{0.5}Fe_{0.5}O_{0.5}F_{1.5}$.

Catalyst Synthesis and Characterizations

A soft chemistry method was chosen to generate $Co_{0.5}Fe_{0.5}O_{0.5}F_{1.5}$. A detailed description can be found in the supporting information. In brief, the catalyst was prepared in a controlled thermal decomposition of a hydrated fluoride precursor (Fig. S1-4 and table S1-10) in mild conditions. The precursor $CoFeF_5(H_2O)_7$ was precipitated by thermally assisted evaporation of a hydrofluoric acid (HF) solution containing metallic salts. The thermal decomposition of $CoFeF_5(H_2O)_7$ was followed by combined thermogravimetric analysis (TGA) and thermodiffraction (Fig. 1a and S5-6). Three thermal events appeared on the TGA curve and thermodiffractograms that correspond to the structural evolution of $CoFeF_5(H_2O)_7$ across four domains (Fig. 1a and b): (i) stability of $CoFeF_5(H_2O)_7$ (RT-100°C, green), (ii) dehydration of $CoFeF_5(H_2O)_7$ (100-220°C, blue), (iii) formation of $Co_{0.5}Fe_{0.5}O_{0.5}F_{1.5}$ with the rutile structure type (220-280°C, purple) and (iv) formation of oxides, CoO and $CoFe_2O_4$ (T°C > 280°C, red). To sum up, $CoFeF_5(H_2O)_7$ undergoes the following decompositions upon thermal treatment according to the reactions (1), (2) and (3). The experimental weight loss values are in good agreement with theoretical values (theoretical wt%, *experimental wt%*):

(1) 100°C-220°C: $Co^{2+}Fe^{3+}F_5(H_2O)_7 \rightarrow Co^{2+}Fe^{3+}F_5 + 7H_2O$ (37.5%, *38.0%*)

(2) 220°C-280°C: $Co^{2+}Fe^{3+}F_5 + H_2O \rightarrow 2Co^{2+}_{0.5}Fe^{3+}_{0.5}O_{0.5}F_{1.5} + 2HF$ (6.6%, *6.7%*)

(3) > 280°C: $2Co^{2+}_{0.5}Fe^{3+}_{0.5}O_{0.5}F_{1.5} + 3/2H_2O \rightarrow ½Co^{2+}O + ½Co^{2+}Fe^{3+}_2O_4 + 3HF$ (9.8%, *9.2%*)

The hydrolysis reactions (2) and (3) are further confirmed by the absence of significant weight loss in the TGA profile performed under dry air at temperatures from 220°C.

The broadening of the Bragg diffraction peaks, compared to the diffraction pattern reveals small coherent diffraction domains (Fig. S7). Indeed, an emerging porosity is observed which is likely related to the precursor's decomposition during which HF and H_2O gas molecules act as a self-generated porogen (Fig. 1c). Upon thermal treatment S_{BET} increases from 3 $m^2.g^{-1}$ to 24 $m^2.g^{-1}$ confirming the porogen effect of the H_2O and HF released. N_2 adsorption/desorption isotherms shows type IV hysteresis corresponding to a mesoporous structure and the BJH pore-size distribution analysis (Fig. 1d) confirms an average pore diameter less than 10 nm, in good agreement with the TEM observation. A disordered model based on metal atoms located in 2a Wyckoff positions (WP) (Co: 50%, Fe: 50%) and the 4f WP statistically occupied by oxygen atoms (25%) and fluorine atoms (75%) was used for Rietveld refinement of $Co_{0.5}Fe_{0.5}O_{0.5}F_{1.5}$ PXRD pattern (space group $P4_2/mnm$). A good fit was obtained in spite of the low crystallinity with the cell parameters: a = b = 4.6916(5) Å, c = 3.1098(3) Å, V = 68.450(1) $Å^3$ (Fig. 1e, S8) and EDS elemental mapping confirmed the resultant CoFe ratio (Fig. S9). ^{57}Fe Mössbauer spectra (Fig. 1f, table S11) and the hyperfine data, in particular δ = 0.39 and 0.46 $mm.s^{-1}$ at 300 and 77K, respectively, are consistent with the presence of only Fe^{3+} species with different atomic environments, resulting from: (i) the presence of octahedral units with shared corners and shared edges, (ii) Fe-Co cationic disorder, and (iii) small crystal grain size, consistent with X-ray analysis. X-ray photoelectron spectroscopy was used to measure the electronic structure of both of the Co and Fe components in $Co_{0.5}Fe_{0.5}O_{0.5}F_{1.5}$. The Fe $2p_{3/2}$ edge could be fit to two components at 710.7 and 712.7 eV (Fig. 1g). These values match that of Fe^{3+} and fall between that of Fe in a pure oxide and a pure fluoride environment. The Co $2p_{3/2}$ peak has a primary feature at 781.7 eV, with a satellite at 786.4 eV which is in between the expected ranges of pure Co fluorides and oxides (Fig. 1h). These measurements illustrate the strong inductive effects imparted through the fluoride components within the lattice hypothesized earlier to influence the catalytic properties of the composite material.

Electrocatalytic Performance

The catalytic properties of $Co_{0.5}Fe_{0.5}O_{0.5}F_{1.5}$ were next evaluated through a host of electrochemical techniques. In a standard 3-electrodes configuration, a cyclic voltammogram (CV) of the catalyst deposited onto a carbon paper electrode in 1M KOH electrolyte showed a redox peak centered at 1.1 V vs. the reversible hydrogen electrode (RHE). This peak was attributed to the Co(II/III) redox couple (Fig. 2a and inset). Electrocatalytic current initiated around 1.4 V_{RHE} requires 220 mV overpotential to reach 10 mA/cm^2 and 265 mV to reach 100 mA/cm^2 at a mass loading of 1 mg/cm^2 using the geometric surface area of the electrode. On the reverse scan, a reductive peak around 1.4 V_{RHE} was observed and attributed to the reduction of Co(IV) back to Co(III) and was more evident with increasingly positive scan limits in the CV (Fig. 2a inset). These assignments are in agreement with previous observations of Co-oxides the literature[26,27] while Fe-oxides typically do not show such redox behavior under these conditions[28]. The oxidation peak of the Co(III/IV) redox couple was not as visible as it was overshadowed by the catalytic current which initiated alongside of the Co(III/IV) oxidation. This signifies that Co(IV) was likely involved in the OER catalytic cycle. We note that there is probably a surface restructuration that occurs as the redox behavior of the 1st CV differs from the 2nd, though no further changes occur afterward (Fig. S10a,b). This indicates that there may be an initial surface restructuration occurring toward a stable surface induced by the application of positive potentials and the environment of Co becomes O/OH-terminated at the surface as suggested by the changes observed on XPS spectra (Fig. S10c-f). Moreover, the peak shift of the Co^{+2} oxidation into Co^{+3} to lower value between the 1st and the 2nd cycle is in agreement with an exchange OH/F at the surface; the M-F is more ionic compared to M-O leading to higher potential[29].

After 1.4 V_{RHE}, the catalytic current rose exceptionally fast and this was reflected in the low Tafel slope of 27 mV/dec (Fig. 2b). A similar Tafel slope was measured if the catalyst was deposited on a glassy carbon rotating disk electrode (RDE) at 0.1 mg/cm^2 in a configuration with minimized mass-transport limitations. In the same configuration, we quantified that mass-activity reached 846 A/g at 300 mV overpotential (Fig. 2c). Similarly, the turnover frequency (TOF) was measured to be 21 /s at this voltage, which was quantified by the redox-active Co atoms that were deduced through integration of the Co(II/III) redox peaks in the CV assuming the Co is indeed the OER active site (Fig. S11). If measured by the total mass loading, the TOF was approximately 0.46 /s, suggesting that approximately 1 out of every 45 Co atoms was electrochemically active. In all, this performance places the $Co_{0.5}Fe_{0.5}O_{0.5}F_{1.5}$ amongst the best reported OER catalysts operating in alkaline electrolyte (Table S12).

The fluorine component was deemed important for the catalytic performance of $Co_{0.5}Fe_{0.5}O_{0.5}F_{1.5}$ because when the catalyst was annealed at 500^{o}C to convert to $CoO/CoFe_2O_4$, the Tafel slope, onset potential and overall activity significantly diminished (Fig. S12). Similarly, the sole carbon paper

support did not significantly contribute to the catalytic current (Fig. S13). The stability of $Co_{0.5}Fe_{0.5}O_{0.5}F_{1.5}$ was next evaluated through chronopotentiometry, switching between several current densities over the course of 27 days without pause (Fig. 2d). While the catalyst was not stable under a concentrated electron beam, prohibiting high-resolution TEM evaluation of the surface after prolonged electrochemical measurements, XPS analysis provided evidence of the surface retention of the Co, Fe, F and O elements (Fig. S10). Finally, rotating ring disk electrode (RRDE) and gas chromatography (GC) measurements confirmed that the current was indeed originating from the OER (Fig. S14). However, a non-negligible quantity of Co and Fe did dissolve into the electrolyte throughout the measurement (Table S13), and this will have to be addressed in following efforts prior to translation of the catalyst into industrial-scale electrolyzers.

Mechanism Study

In order to probe the reaction mechanism and understand the roles of Co and Fe atoms for $Co_{0.5}Fe_{0.5}O_{0.5}F_{1.5}$, we first performed density functional theory (DFT) computations. Here, we chose (110) facet because of its lowest surface energy and thus the most stable surface in rutile structures.[24,30] Two reaction pathways are considered here, adopting different O–O bond formation strategies, which are the water nucleophilic attack (WNA) and the interaction of two metal-oxo units (I2M) (Fig. S15). These two mechanisms are reported to be the primary reaction pathways for the OER.[31] Two model structures of $Co_{0.5}Fe_{0.5}O_{0.5}F_{1.5}$ are proposed for the DFT simulations to shed light on the role of Co and Fe species, where the switch between Co and Fe atoms takes place intermittently (denoted as CoFeOF(110)-1) or continuously (denoted as CoFeOF(110)-2). Following the WNA and I2M mechanisms, we tested each intermediate on multiple active sites for each model catalyst, where only the most stable configurations were shown (Fig. 3a and b). For both model catalysts, we noticed that the adsorbed oxyhydroxide intermediate (*OOH) is unstable and tends to decompose into adsorbed oxygen atom (*O) and adsorbed hydroxide (*OH). We also observed that for CoFeOF(110)-1, when two *O are placed on the surface, they are prone to relocate at a bridge position where either of them is between Co and Fe atoms. We assume that two *O intermediates favor similar local environments (i.e., both bridge positions are between Co and Fe versus two bridge positions are between different two metal atoms) so that the energy of the system can reach its optimum through relocation. After the relocation of two *O, one *O in either adjacent unit cell comes closer to each other to form the *O-O* coupling between two Fe atoms.

From the energy profiles (Fig. 3c and f), it is apparent that the I2M mechanism has a lower energy barrier (4.02 and 3.51 eV, for structures 1 and 2, respectively) for its rate-limiting step (RLS, which is the desorption of O_2) and thus is more favorable than the WNA mechanism (7.77 and 7.91 eV, for structures 1 and 2, respectively) for both model catalysts without any applied potentials (i.e., at

U = 0 V). For both WNA and I2M mechanisms, their first two steps are the same electrochemical reactions with electron transfer. However, the last two steps in the I2M mechanism are chemical reactions without any electron transfer, whereas the last two steps in the WNA mechanism still contain electron transfer. Therefore, a large enough applied potential can theoretically suppress the limiting energy barrier in the WNA mechanism without any impact on the limiting energy barrier in the I2M mechanism to compel the two limiting energy barriers to equal. However, due to the large difference between the two limiting energy barriers at U = 0 V, only if an applied potential that is greater than 3.75 V for CoFeOF(110)-1 and 4.40 V for CoFeOF(110)-2, allows the reaction pathway shift from the I2M to the WNA mechanism. Since the applied potentials employed in this study are much smaller than 3.75 V and 4.40 V, we posit that the I2M mechanism containing an *O-O* coupling is the reaction pathway for $Co_{0.5}Fe_{0.5}O_{0.5}F_{1.5}$ catalyst.

Furthermore, a comparison of the energy profiles on both model catalysts, illustrates that CoFeOF(110)-2 has a lower limiting energy barrier at U = 0 V and requires a higher applied potential to shift from the I2M pathway to the WNA pathway. This implies that the structure of CoFeOF(110)-2 following the WNA pathway is more favorable for the OER, and the existence of Co benefits the reaction. To further shed light on the reaction mechanism, we calculated the Bader charge distribution and the charge density difference to analyze the *O-O* coupling sites for CoFeOF(110)-1 (Fig. 3d and e) and CoFeOF(110)-2 (Fig. 3g and h). The cyan contours around the metal atoms and the yellow regions around the *O-O* indicate that the metal atoms lose electrons, while the *O-O* entities gain electrons. This can be also concluded from the Bader charge distribution. More importantly, the Bader charger distribution implies that Fe atoms lose more electrons than Co atoms, which is further confirmed by the fact that the *O connected to Fe gains more electrons. This means the interaction between Fe and *O is stronger than between Co and *O. The lowest adsorption energy of O_2 at the bridge sites between two adjacent cations: Fe/Fe, Fe/Co, and Co/Co (Fig. S16) was found for Fe/Co. This feature confirms that the unbalanced interactions between Co-O and Fe-O results in unstable *O-O* on CoFeOF(110)-2, thereby making O_2 desorption easier. This inference is also implied from the additional Bader charge distribution and the charge density difference (Fig. S17), which illustrates the uneven charge density distribution in *O-O* between Co and Fe due to the different capabilities of Co and Fe to donate electrons to *O-O*. DFT calculations performed herein demonstrate that the I2M mechanism containing an *O-O* coupling is the most favorable reaction pathway and the O_2 desorption is the RLS. In addition, DFT results posit that both Co and Fe play a critical role in the enhanced performance of the OER.

We next took to further elucidating the mechanism of the OER on $Co_{0.5}Fe_{0.5}O_{0.5}F_{1.5}$ catalyst surfaces through pH-dependent electrochemical experiments. CVs of the catalyst were recorded from pH 11 to nominally pH 14 (Fig. 4a). At pH 11, the current attributed to Co redox peaks was considerably lower until approximately pH 12, whereas the reduction of Co(IV) increased continually

until pH 14. Only at pH 14, the same amount of charge was integrated under the Co(IV) reduction as the Co(III) reduction (Fig. 4b). In addition to the rise in Co(IV), the catalytic current also increased more rapidly at higher pH electrolytes, quantified here by a decrease in Tafel slope (Fig. 4c). Finally, the absolute potential (here plotted on vs. the Standard Hydrogen Electrode, SHE) of the Co redox potentials and the catalytic current exhibited differing shifts as a function of electrolyte pH (Fig. 4d). First, the Co(II/III) redox couple shifted 91 mV/pH, indicative of a $2e^-$, $3H^+$ process. This super-Nernstian behavior often signifies that the redox transition is coupled with not only the deprotonation of a group adsorbed on the Co, but also with a more extended deprotonation of sites within the lattice with a pKa of approximately 12, as at this pH value, the magnitude of the redox wave stops increasing[26,32,33]. On the other hand, the Co(III/IV) redox wave shifted 63 mV/pH, indicating that this process was a simple $1e^-$, $1H^+$ (or $2e^-$, $2H^+$) process. The current necessary to attain 10 mA/cm^2, as measured in galvanostatic mode, showed a shift of 102 mV/pH. Such a dependence of pH on OER catalysis has previously been attributed to a decoupling of proton transfer, electron transfer, and catalytic steps in the OER cycle and has often implied the active role of lattice oxygen in reaction pathway[34,35]. The next measurement in the series was the use of chemical probes to deduce the presence of particular surface intermediates. We first introduced 1M methanol into the electrolyte as adsorbed nucleophilic *OH groups on metal oxide surfaces were previously found to react with alcohols[36]. Indeed, we observed a slow onset of methanol oxidation just past the Co(II/III) redox transition pointing to the initiation of reactive *OH coverage at this potential value (Fig. 4e). On the other hand, using 1M tetramethylammonium hydroxide (TMAOH) as the electrolyte, previously argued to specifically interact with active oxygen species and thus hinder the OER cycle[37,38], shifted the Co(II/III) redox peak and increased the Tafel slope to 34 mV/dec. This provides evidence for interactions between the $Co_{0.5}Fe_{0.5}O_{0.5}F_{1.5}$ surface and TMA ions, likely through activated oxygen species.

Finally, to probe chemical nature of the rate-limiting step in the OER cycle, we utilized H/D and $^{16}O/^{18}O$ isotope measurements. In comparing the CV measurements (Fig. 4f) and the resultant Tafel slopes (Fig. 4g), there were minimal changes between the catalyst in KOH and KOD electrolytes, implying that O-H/D cleavage not involved in the rate limiting step. However, when using $K^{18}OH$, the resultant current density dropped significantly and the Tafel slope increased by approximately 15 mV/dec, to 42 mV/dec which indicates that oxygen atoms are the sole species involved in the rate limiting step and the catalytic cycle is pushed away from the conventional one with proton-coupled electron transfer (PCET) steps often involving the breaking of a O-H bond[6].

In a complementary thrust, *in operando* Raman spectroscopy was performed as this type of vibrational spectroscopy can help to elucidate changes in catalyst surface structure through the course of the reaction cycle (Fig. 4h). We focused on the spectral region of 100-900 cm^{-1}, where M-M and M-

O vibrational modes are typically seen. While there is not an established literature base that can be used to unambiguously assign bands to the particular vibrational modes of $Co_{0.5}Fe_{0.5}O_{0.5}F_{1.5}$, we probe the changes in the spectra and reference vs. previous Raman observations of OER-active cobalt and iron-based catalysts. At open circuit, bands at 342, 513, 620, 687, 735 and 809 cm^{-1} were observed. Upon the application of oxidizing potentials, the band at 513 redshifted to 501 cm^{-1}, new band components arose at 590 and 580 cm^{-1}, and a band at 687 cm^{-1} rose and fell. A band that progressively shifted from 609 to 580 cm^{-1} with positive potentials has previously been observed for CoO_x thin films as Co underwent Co(II/III) and Co(III/IV) redox transitions[39]. A reasonable assignment would also be such changes in our spectra to Co-O species that are oxidized at 1.1V and 1.4 V. The emergence of a band at 503 cm^{-1} may also match that of CoOOH[40,41]. The potentials at which these changes occurred matched that of the Co(II/III) and the Co(III/IV) oxidations and onset of OER catalysis. In addition, the spectral features observed for $Co_{0.5}Fe_{0.5}O_{0.5}F_{1.5}$ did not particularly match any spectra for iron oxide phases[42,43].

With above data in mind, we were able to construct a plausible mechanism for the OER on $Co_{0.5}Fe_{0.5}O_{0.5}F_{1.5}$ surfaces (Fig. 5). First, a $2e^-$, $3H^+$ process occurs at 1.1 V_{RHE} to generate Co(III) and deprotonate adsorbed water groups to *OH. Next, the Co(III)-OH becomes further oxidized at 1.4V_{RHE} to Co(IV)-O^-, here illustrated as a $2e^-$, $2H^+$ process. However, the presence of Co(IV) is not enough to achieve highly efficient OER catalysis as Co(IV) was observed even at pH 11, in the absence of significant catalysis. Instead, there is another deprotonation step, likely that of a bridging oxygen atom, either between Co and Co or Co and Fe. This deprotonation, along with the $2e^-$, $2H^+$ Co(III/IV) transition give rise to the observed 102 mV/pH, $2e^-$, $3H^+$, rate dependence of the OER of $Co_{0.5}Fe_{0.5}O_{0.5}F_{1.5}$ catalysts. The rapid drop in Tafel slope until pH 12 indicates that the pKa of this bridging oxygen at 1.4V_{RHE} is approximately 12.

Following the bridging oxygen deprotonation, is the O-O bond formation, and finally the O_2 release. The latter is the rate limiting step as evidenced through the computational efforts and O^{18} isotopic measurements. A plausible set of electron and water/hydroxide transfer steps was added finally to complete the OER cycle. Overall, the data implies a decoupling of key proton transfer, electron transfer and chemical steps and a lattice oxygen involving mechanism on $Co_{0.5}Fe_{0.5}O_{0.5}F_{1.5}$, a departure from the conventional route of purely proton-coupled electron transfer steps, though one that is highly efficient. Further, the active site here is deemed to be a Co-Fe bimolecular site.

Returning back to conventional limitations in OER catalysis, this mechanism, which circumvents the standard PCET route, appears to be the origin of the $Co_{0.5}Fe_{0.5}O_{0.5}F_{1.5}$ exceptional performance. In fact, in recent years, key high performing alkaline OER catalysts also bypassed the standard PCET mechanism.[27,32,35,37,44,45] While the exact nature of every step and free-energy landscape of the OER on different crystal facets and active sites is not yet elucidated, nor are the precise effects

of the fluorine components on the Co and Fe species deciphered, there are many routes forward to take in understanding this system and building upon the extracted insights to design next-generation materials. Both soft and hard X-ray absorption spectroscopies would be key in capturing the element-specific electronic changes throughout the catalytic cycle. Vibrational spectroscopy, especially with the aid of isotope labelling and time-resolved measurements would also be instrumental in detecting every intermediate in the reaction pathway to render a closer match between the proposed model and reality. In the direction of OER catalyst innovation, the exploration of novel anionic components substituted into transition metal oxides has shown to be a fruitful avenue to pursue and one can point to recently innovated oxyhalide catalysts.[13,15,16,19]

Concluding Remarks

The work put forth in this study highlights the utility of exploring hetero-anionic composition in the discovery of efficient catalytic materials. A mixed anion compound, $Co_{0.5}Fe_{0.5}O_{0.5}F_{1.5}$, was fabricated through a controlled thermal conversion route and, the resultant material exhibited exceptionally high activity for the OER. A set of mechanistic investigations were carried out to elucidate key steps in the reaction mechanism and through this process, we found the OER proceeding through a super-Nernstian pH-dependent process. In all, the research illustrated here is envisioned to open pathways in electrocatalyst design through the exploration of multi-metallic oxyfluoride materials that in key cases can surpass the activity of the state-of-the-art oxides. Mechanistically, exciting questions have yet to be answered, such as the elucidation of electronic structure changes and the precise interplay of Co, Fe, F, and O components in the lattice, for which both theoretical modelling and X-ray absorption spectroscopy can potentially be instrumental. In the context of the OER, while $Co_{0.5}Fe_{0.5}O_{0.5}F_{1.5}$ surpasses the performance of most known Co-based catalysts, there is no reason that it has to be the most active oxyfluoride. Thus, many promising avenues in nanostructuration, structural and compositional modulation may yield an even more active next-generation material.

Experimental Procedures:

Resource Availability:

Lead contact: Further information and requests for resources and reagents should be directed to and will be fulfilled by the lead contact, Nikolay Kornienko (nikolay.kornienko@umontreal.ca).

Materials availability: Any materials used are freely available from the lead contact upon request.

Data and code availability: Data is freely available upon request from the lead contact. No code was generated. Full experimental procedures are provided in the supplemental information.

Acknowledgments:

J.L. thanks CNRS for funding the EMERGENCE@INC2020 Project (H_2FLU). The authors attached to IMMM gratefully acknowledge the users responsible of the technical platforms "X-ray Diffusion and Diffraction" and "Electron Microscopy" of IMMM (Le Mans University). N.K. acknowledges NSERC for its Discovery Grant RGPIN-2019-05927. All authors thank FRQNT Samuel de Champlain program, award 293526. A.S. acknowledges NSERC for its Discovery Grant RGPIN-2020-04960 and Canada Research Chair (950-23288). Computations in this research were enabled in part by support provided by Calcul Quebec and Compute Canada.

Author Contributions:

Z.G-B, A.G., R.M., J-M.G., A.H-R., V.M., and J.L. carried out the catalyst synthesis and physical characterization. N.K., Y.Z. and D.C. carried out electrochemical and spectroscopic experiments. X.W. and A.S. carried out computational modelling.

Declaration of Interests:

A patent has been filed regarding the catalyst developed in this manuscript.

References:

1. Fawzy, S., Osman, A.I., Doran, J., and Rooney, D.W. (2020). Strategies for mitigation of climate change: a review. Environ. Chem. Lett. *18*, 2069-2094. 10.1007/s10311-020-01059-w.
2. Stamenkovic, V.R., Strmcnik, D., Lopes, P.P., and Markovic, N.M. (2017). Energy and fuels from electrochemical interfaces. Nat. Mater. *16*, 57-69. 10.1038/nmat4738.
3. Montoya, J.H., Seitz, L.C., Chakthranont, P., Vojvodic, A., Jaramillo, T.F., and Nørskov, J.K. (2017). Materials for solar fuels and chemicals. Nat. Mater. *16*, 70-81. 10.1038/nmat4778.
4. Electrochemistry for a Sustainable World. (2020). Electrochem. Soc. Interface *29*, 41-42. 10.1149/2.f05203if.
5. Burke, M.S., Enman, L.J., Batchellor, A.S., Zou, S., and Boettcher, S.W. (2015). Oxygen Evolution Reaction Electrocatalysis on Transition Metal Oxides and (Oxy)hydroxides: Activity Trends and Design Principles. Chem. Mater. *27*, 7549-7558. 10.1021/acs.chemmater.5b03148.
6. Hu, C., Zhang, L., and Gong, J. (2019). Recent progress made in the mechanism comprehension and design of electrocatalysts for alkaline water splitting. Energy Environ. Sci. *12*, 2620-2645. 10.1039/C9EE01202H.
7. Suen, N.-T., Hung, S.-F., Quan, Q., Zhang, N., Xu, Y.-J., and Chen, H.M. (2017). Electrocatalysis for the oxygen evolution reaction: recent development and future perspectives. Chem. Soc. Rev. *46*, 337-365. 10.1039/C6CS00328A.
8. Song, F., Bai, L., Moysiadou, A., Lee, S., Hu, C., Liardet, L., and Hu, X. (2018). Transition Metal Oxides as Electrocatalysts for the Oxygen Evolution Reaction in Alkaline Solutions: An Application-Inspired Renaissance. J. Am. Chem. Soc. *140*, 7748-7759. 10.1021/jacs.8b04546.

9. Song, J., Wei, C., Huang, Z.-F., Liu, C., Zeng, L., Wang, X., and Xu, Z.J. (2020). A review on fundamentals for designing oxygen evolution electrocatalysts. Chem. Soc. Rev. *49*, 2196-2214. 10.1039/C9CS00607A.
10. Hunter, B.M., Gray, H.B., and Müller, A.M. (2016). Earth-Abundant Heterogeneous Water Oxidation Catalysts. Chem. Rev. *116*, 14120-14136. 10.1021/acs.chemrev.6b00398.
11. Peugeot, A., Creissen, C.E., Karapinar, D., Tran, H.N., Schreiber, M., and Fontecave, M. (2021). Benchmarking of oxygen evolution catalysts on porous nickel supports. Joule *5*, 1281-1300. https://doi.org/10.1016/j.joule.2021.03.022.
12. Kuznetsov, D.A., Han, B., Yu, Y., Rao, R.R., Hwang, J., Román-Leshkov, Y., and Shao-Horn, Y. (2018). Tuning Redox Transitions via Inductive Effect in Metal Oxides and Complexes, and Implications in Oxygen Electrocatalysis. Joule *2*, 225-244. https://doi.org/10.1016/j.joule.2017.11.014.
13. Lemoine, K., Lhoste, J., Hémon-Ribaud, A., Heidary, N., Maisonneuve, V., Guiet, A., and Kornienko, N. (2019). Investigation of mixed-metal (oxy)fluorides as a new class of water oxidation electrocatalysts. Chem. Sci. *10*, 9209-9218. 10.1039/C9SC04027G.
14. Liang, K., Guo, L., Marcus, K., Zhang, S., Yang, Z., Perea, D.E., Zhou, L., Du, Y., and Yang, Y. (2017). Overall Water Splitting with Room-Temperature Synthesized NiFe Oxyfluoride Nanoporous Films. ACS Catal. *7*, 8406-8412. 10.1021/acscatal.7b02991.
15. Fan, X., Liu, Y., Chen, S., Shi, J., Wang, J., Fan, A., Zan, W., Li, S., Goddard, W.A., and Zhang, X.-M. (2018). Defect-enriched iron fluoride-oxide nanoporous thin films bifunctional catalyst for water splitting. Nat. Commun, *9*, 1809. 10.1038/s41467-018-04248-y.
16. Chen, P., Zhou, T., Wang, S., Zhang, N., Tong, Y., Ju, H., Chu, W., Wu, C., and Xie, Y. (2018). Dynamic Migration of Surface Fluorine Anions on Cobalt-Based Materials to Achieve Enhanced Oxygen Evolution Catalysis. Angew. Chem. Int. Ed. *57*, 15471-15475. https://doi.org/10.1002/anie.201809220.
17. Xue, Y., Wang, Y., Liu, H., Yu, X., Xue, H., and Feng, L. (2018). Electrochemical oxygen evolution reaction catalyzed by a novel nickel–cobalt-fluoride catalyst. Chem. Commun. *54*, 6204-6207. 10.1039/C8CC03223H.
18. Han, H., Woo, J., Hong, Y.-R., Chung, Y.-C., and Mhin, S. (2019). Polarized Electronic Configuration in Transition Metal–Fluoride Oxide Hollow Nanoprism for Highly Efficient and Robust Water Splitting. ACS Appl. Energy Mater. *2*, 3999-4007. 10.1021/acsaem.9b00449.
19. Wang, J., Kim, S.-J., Liu, J., Gao, Y., Choi, S., Han, J., Shin, H., Jo, S., Kim, J., Ciucci, F., et al. (2021). Redirecting dynamic surface restructuring of a layered transition metal oxide catalyst for superior water oxidation. Nat. Catal. *4*, 212-222. 10.1038/s41929-021-00578-1.
20. Huang, Z.-F., Song, J., Dou, S., Li, X., Wang, J., and Wang, X. (2019). Strategies to Break the Scaling Relation toward Enhanced Oxygen Electrocatalysis. Matter *1*, 1494-1518. https://doi.org/10.1016/j.matt.2019.09.011.
21. Brink, F.J., Withers, R.L., and Norén, L. (2001). Nonstoichiometric, Rutile-Type, Solid Solutions in the FeIIF2–FeIIIOF System. J. Solid State Chem. *161*, 31-37. https://doi.org/10.1006/jssc.2001.9243.
22. Fan, X., Hu, E., Ji, X., Zhu, Y., Han, F., Hwang, S., Liu, J., Bak, S., Ma, Z., Gao, T., et al. (2018). High energy-density and reversibility of iron fluoride cathode enabled via an intercalation-extrusion reaction. Nat. Commun, *9*, 2324. 10.1038/s41467-018-04476-2.
23. Zhou, H., Nanda, J., Martha, S.K., Adcock, J., Idrobo, J.C., Baggetto, L., Veith, G.M., Dai, S., Pannala, S., and Dudney, N.J. (2013). Formation of Iron Oxyfluoride Phase on the Surface of Nano-Fe3O4 Conversion Compound for Electrochemical Energy Storage. J. Phys. Chem. Lett. *4*, 3798-3805. 10.1021/jz402017h.
24. Zhu, J., and Deng, D. (2015). Wet-Chemical Synthesis of Phase-Pure FeOF Nanorods as High-Capacity Cathodes for Sodium-Ion Batteries. Angew. Chem. Int. Ed. *54*, 3079-3083. https://doi.org/10.1002/anie.201410572.
25. Lemoine, K., Zhang, L., Grenèche, J.-M., Hémon-Ribaud, A., Leblanc, M., Guiet, A., Galven, C., Tarascon, J.-M., Maisonneuve, V., and Lhoste, J. (2019). New Amorphous Iron-Based Oxyfluorides as Cathode Materials for High-Capacity Lithium-Ion Batteries. J. Phys. Chem. C *123*, 21386-21394. 10.1021/acs.jpcc.9b06055.

26. Moysiadou, A., Lee, S., Hsu, C.-S., Chen, H.M., and Hu, X. (2020). Mechanism of Oxygen Evolution Catalyzed by Cobalt Oxyhydroxide: Cobalt Superoxide Species as a Key Intermediate and Dioxygen Release as a Rate-Determining Step. J. Am. Chem. Soc. *142*, 11901-11914. 10.1021/jacs.0c04867.
27. Bergmann, A., Martinez-Moreno, E., Teschner, D., Chernev, P., Gliech, M., de Araújo, J.F., Reier, T., Dau, H., and Strasser, P. (2015). Reversible amorphization and the catalytically active state of crystalline Co3O4 during oxygen evolution. Nat. Commun, *6*, 8625. 10.1038/ncomms9625.
28. Burke, M.S., Kast, M.G., Trotochaud, L., Smith, A.M., and Boettcher, S.W. (2015). Cobalt–Iron (Oxy)hydroxide Oxygen Evolution Electrocatalysts: The Role of Structure and Composition on Activity, Stability, and Mechanism. J. Am. Chem. Soc. *137*, 3638-3648. 10.1021/jacs.5b00281.
29. Zu, C.-X., and Li, H. (2011). Thermodynamic analysis on energy densities of batteries. Energy Environ. Sci. *4*, 2614-2624. 10.1039/C0EE00777C.
30. Hanaor, D.A.H., Xu, W., Ferry, M., and Sorrell, C.C. (2012). Abnormal grain growth of rutile TiO2 induced by ZrSiO4. J. Cryst. Growth *359*, 83-91. https://doi.org/10.1016/j.jcrysgro.2012.08.015.
31. Craig, M.J., Coulter, G., Dolan, E., Soriano-López, J., Mates-Torres, E., Schmitt, W., and García-Melchor, M. (2019). Universal scaling relations for the rational design of molecular water oxidation catalysts with near-zero overpotential. Nat. Commun, *10*, 4993. 10.1038/s41467-019-12994-w.
32. Bai, L., Lee, S., and Hu, X. (2021). Spectroscopic and Electrokinetic Evidence for a Bifunctional Mechanism of the Oxygen Evolution Reaction**. Angew. Chem. Int. Ed. *60*, 3095-3103. https://doi.org/10.1002/anie.202011388.
33. Bediako, D.K., Surendranath, Y., and Nocera, D.G. (2013). Mechanistic Studies of the Oxygen Evolution Reaction Mediated by a Nickel–Borate Thin Film Electrocatalyst. J. Am. Chem. Soc. *135*, 3662-3674. 10.1021/ja3126432.
34. Grimaud, A., Diaz-Morales, O., Han, B., Hong, W.T., Lee, Y.-L., Giordano, L., Stoerzinger, K.A., Koper, M.T.M., and Shao-Horn, Y. (2017). Activating lattice oxygen redox reactions in metal oxides to catalyse oxygen evolution. Nat. Chem. *9*, 457-465. 10.1038/nchem.2695.
35. Zhang, N., Feng, X., Rao, D., Deng, X., Cai, L., Qiu, B., Long, R., Xiong, Y., Lu, Y., and Chai, Y. (2020). Lattice oxygen activation enabled by high-valence metal sites for enhanced water oxidation. Nat. Commun, *11*, 4066. 10.1038/s41467-020-17934-7.
36. Tao, H.B., Xu, Y., Huang, X., Chen, J., Pei, L., Zhang, J., Chen, J.G., and Liu, B. (2019). A General Method to Probe Oxygen Evolution Intermediates at Operating Conditions. Joule *3*, 1498-1509. https://doi.org/10.1016/j.joule.2019.03.012.
37. Huang, Z.-F., Song, J., Du, Y., Xi, S., Dou, S., Nsanzimana, J.M.V., Wang, C., Xu, Z.J., and Wang, X. (2019). Chemical and structural origin of lattice oxygen oxidation in Co–Zn oxyhydroxide oxygen evolution electrocatalysts. Nat. Energy *4*, 329-338. 10.1038/s41560-019-0355-9.
38. Yang, C., Fontaine, O., Tarascon, J.-M., and Grimaud, A. (2017). Chemical Recognition of Active Oxygen Species on the Surface of Oxygen Evolution Reaction Electrocatalysts. Angew. Chem. Int. Ed. *56*, 8652-8656. https://doi.org/10.1002/anie.201701984.
39. Yeo, B.S., and Bell, A.T. (2011). Enhanced Activity of Gold-Supported Cobalt Oxide for the Electrochemical Evolution of Oxygen. J. Am. Chem. Soc. *133*, 5587-5593. 10.1021/ja200559j.
40. Alrehaily, L.M., Joseph, J.M., Biesinger, M.C., Guzonas, D.A., and Wren, J.C. (2013). Gamma-radiolysis-assisted cobalt oxide nanoparticle formation. Phys. Chem. Chem. Phys. *15*, 1014-1024. 10.1039/C2CP43094K.
41. Yang, J., Liu, H., Martens, W.N., and Frost, R.L. (2010). Synthesis and Characterization of Cobalt Hydroxide, Cobalt Oxyhydroxide, and Cobalt Oxide Nanodiscs. J. Phys. Chem. C *114*, 111-119. 10.1021/jp908548f.
42. Bersani, D., Lottici, P.P., and Montenero, A. (1999). Micro-Raman investigation of iron oxide films and powders produced by sol–gel syntheses. J. Raman Spectrosc. *30*, 355-360. https://doi.org/10.1002/(SICI)1097-4555(199905)30:5<355::AID-JRS398>3.0.CO;2-C.

43. de Faria, D.L.A., Venâncio Silva, S., and de Oliveira, M.T. (1997). Raman microspectroscopy of some iron oxides and oxyhydroxides. J. Raman Spectrosc. *28*, 873-878. https://doi.org/10.1002/(SICI)1097-4555(199711)28:11<873::AID-JRS177>3.0.CO;2-B.
44. Grimaud, A., Hong, W.T., Shao-Horn, Y., and Tarascon, J.M. (2016). Anionic redox processes for electrochemical devices. Nat. Mater. *15*, 121-126. 10.1038/nmat4551.
45. Zhang, N., and Chai, Y. (2021). Lattice oxygen redox chemistry in solid-state electrocatalysts for water oxidation. Energy Environ. Sci. 10.1039/D1EE01277K.

Figure and scheme titles and legends

Figure 1. **Catalyst synthesis and Characterization.** TGA analyses under dry air (line dashed) and ambient air of $CoFeF_5(H_2O)_7$ **(a)**. Thermal evolution of the X-ray diffractograms under ambient air of $CoFeF_5(H_2O)_7$ **(b)**. TEM micrographs **(c)** and N_2 adsorption/desorption isotherm (the inset corresponds to the BJH pore size distribution analyzed from the desorption branch) **(d)** of $Co_{0.5}Fe_{0.5}O_{0.5}F_{1.5}$. Rietveld refinement of the PXRD pattern of $Co_{0.5}Fe_{0.5}O_{0.5}F_{1.5}$ with the inset illustrating the [100] projection of $Co_{0.5}Fe_{0.5}O_{0.5}F_{1.5}$ structure **(e)**. ^{57}Fe Mössbauer spectra recorded at 2 $mm.s^{-1}$ at 300 and 77K **(f)**. XPS spectra illustrate the electron withdrawing effects of the fluoride components on the Fe **(g)** and Co **(h)** components.

Figure 2. Catalyst performance. CV curves of $Co_{0.5}Fe_{0.5}O_{0.5}F_{1.5}$, with the inset representing CVs at different scan limits. $Co_{0.5}Fe_{0.5}O_{0.5}F_{1.5}$ exhibits 2 redox peaks, at 1.1 V_{RHE} and 1.4 V_{RHE}, just prior to the onset of the OER (1st cycle is removed) (a). Tafel plot of $Co_{0.5}Fe_{0.5}O_{0.5}F_{1.5}$ obtained on carbon paper and glassy carbon RDE electrodes; similar Tafel slopes are measured on both substrates (b). Plot of the mass activities and TOF as a function of the applied potential, a mass activity of 846 A/g and TOF of 21/s were recorded at 300 mV overpotential (c). Chronopotentiometric evaluation of $Co_{0.5}Fe_{0.5}O_{0.5}F_{1.5}$: the activity did not noticeably decrease through 27 days of measurement (d).

Figure 3. Computational Modelling. Comparison of the WNA and I2M mechanisms for CoFeOF(110)-1 **(a)** and CoFeOF(110)-2 **(b)**. The cobalt, iron, oxygen, and fluorine atoms are marked as blue, gold, red, and silver, respectively. Energy profiles for CoFeOF(110)-1 **(c)** and CoFeOF(110)-2 **(f)** with applied potentials. The highlights represent the rate-limiting steps with the values of the relevant energy barriers labelled. The Bader charge distribution and the corresponding charge density difference at the *O-O* coupling sites for CoFeOF(110)-1 **(d, e)** and CoFeOF(110)-2 **(g, h)**. The yellow and cyan contours denote electron accumulation and depletion, respectively.

Figure 4. Analytical measurements. Analysis of the CVs of $Co_{0.5}Fe_{0.5}O_{0.5}F_{1.5}$ at different pH electrolyte were used to unveil trends in Co redox and catalysis (**a**). As the pH increased, so did the quantity of Co(III) and Co(IV) observed (**b**). The increase in pH was coupled to an enhanced catalytic process, evidenced by the decrease in Tafel slope (**c**). Interestingly, the Co redox peaks and catalytic current exhibited both Nernstian and super-Nernstian pH shifts (**d**). *OH was evidenced above $1.1V_{RHE}$ through an increase in current in the presence of methanol while active oxygen species were evidenced when TMA cations were added to the electrolyte (**e**). Isotope measurements (**f, g**) indicated that the catalyst performance is most hampered by $K^{18}OH$ rather than KOD. Raman spectroscopy indicated hydration of $Co_{0.5}Fe_{0.5}O_{0.5}F_{1.5}$ upon the application of positive potentials (**h**) shows three distinct species forming as a function of applied potential.

Figure 5. Mechanism. Proposed reaction pathway on $Co_{0.5}Fe_{0.5}O_{0.5}F_{1.5}$ surfaces. Note: surface charges are omitted for simplicity.

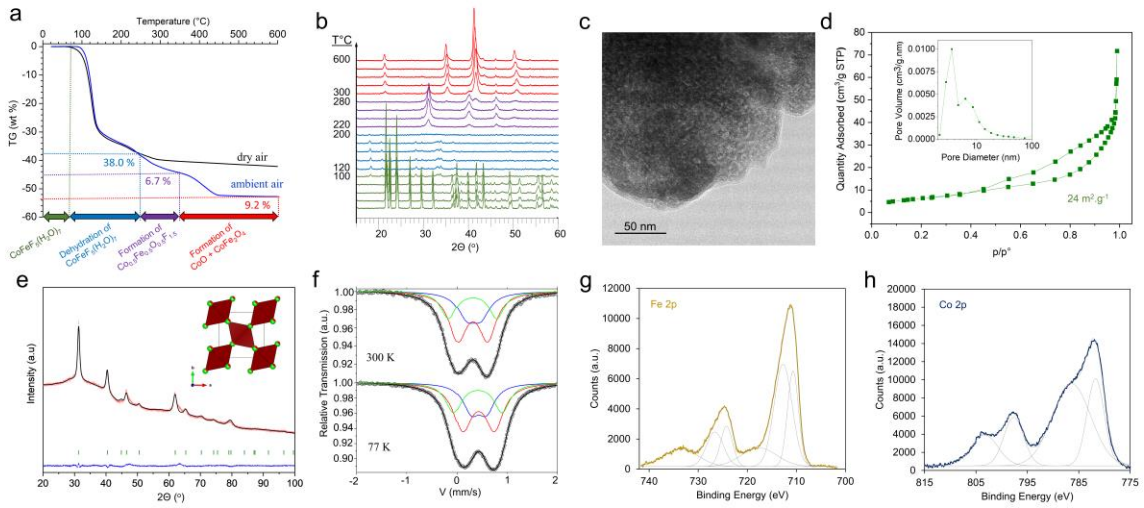
a
Temperature (°C)
TG (wt %)
38.0 %
6.7 %
9.2 %
dry air
ambient air
b
T°C
2Θ (°)
c
50 nm
d
Quantity Adsorbed (cm³/g STP)
Pore Volume (cm³/g.nm)
Pore Diameter (nm)
24 m².g⁻¹
p/p°
e
Intensity (a.u)
2Θ (°)
f
Relative Transmission (a.u.)
300 K
77 K
V (mm/s)
g
Fe 2p
Counts (a.u.)
Binding Energy (eV)
h
Co 2p
Counts (a.u.)
Binding Energy (eV)

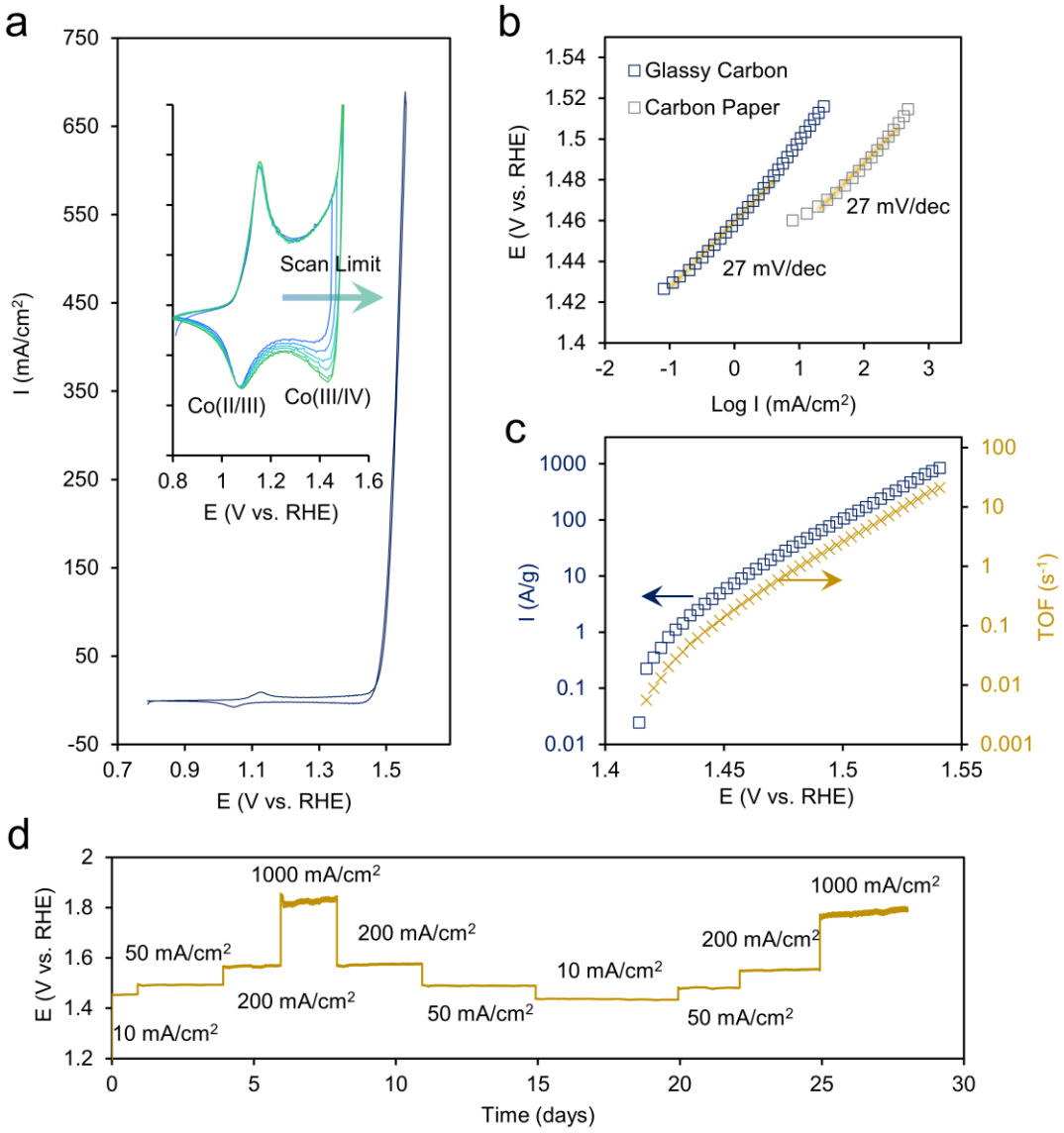
a
I (mA/cm²)
E (V vs. RHE)
Scan Limit
Co(II/III)
Co(III/IV)
b
Glassy Carbon
Carbon Paper
27 mV/dec
27 mV/dec
E (V vs. RHE)
Log I (mA/cm²)
c
I (A/g)
TOF (s⁻¹)
E (V vs. RHE)
d
E (V vs. RHE)
Time (days)
10 mA/cm²
50 mA/cm²
200 mA/cm²
1000 mA/cm²
50 mA/cm²
10 mA/cm²
200 mA/cm²
50 mA/cm²
200 mA/cm²
1000 mA/cm²

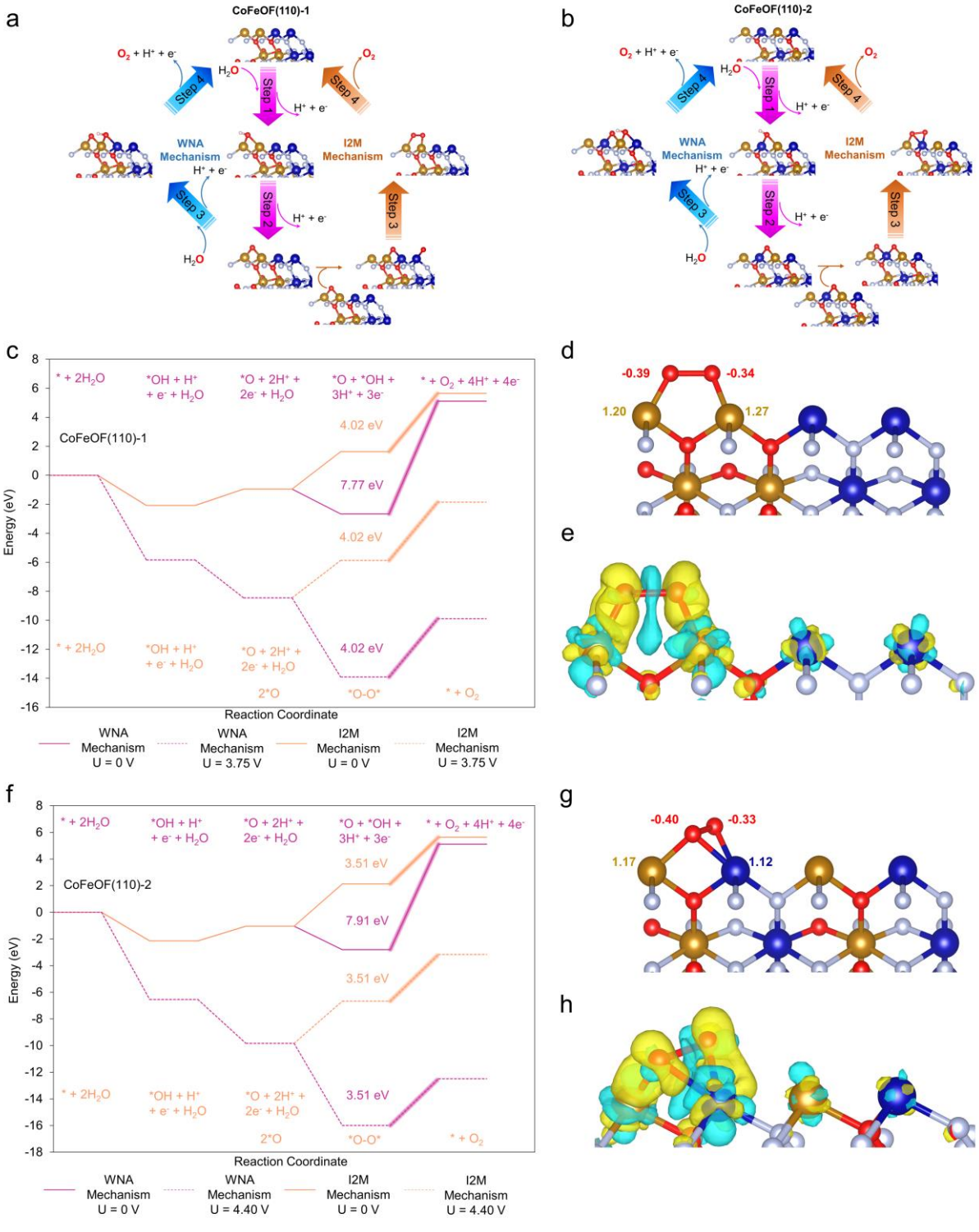
a
CoFeOF(110)-1
$O_2 + H^+ + e^-$
H_2O
O_2
Step 4
Step 1
Step 2
Step 3
$H^+ + e^-$
WNA Mechanism
I2M Mechanism
b
CoFeOF(110)-2
c
CoFeOF(110)-1
$* + 2H_2O$
$*OH + H^+ + e^- + H_2O$
$*O + 2H^+ + 2e^- + H_2O$
$*O + *OH + 3H^+ + 3e^-$
$* + O_2 + 4H^+ + 4e^-$
4.02 eV
7.77 eV
4.02 eV
4.02 eV
2*O
O-O
Energy (eV)
Reaction Coordinate
WNA Mechanism U = 0 V
WNA Mechanism U = 3.75 V
I2M Mechanism U = 0 V
I2M Mechanism U = 3.75 V
d
-0.39
-0.34
1.20
1.27
e
f
CoFeOF(110)-2
3.51 eV
7.91 eV
3.51 eV
3.51 eV
WNA Mechanism U = 0 V
WNA Mechanism U = 4.40 V
I2M Mechanism U = 0 V
I2M Mechanism U = 4.40 V
g
-0.40
-0.33
1.17
1.12
h

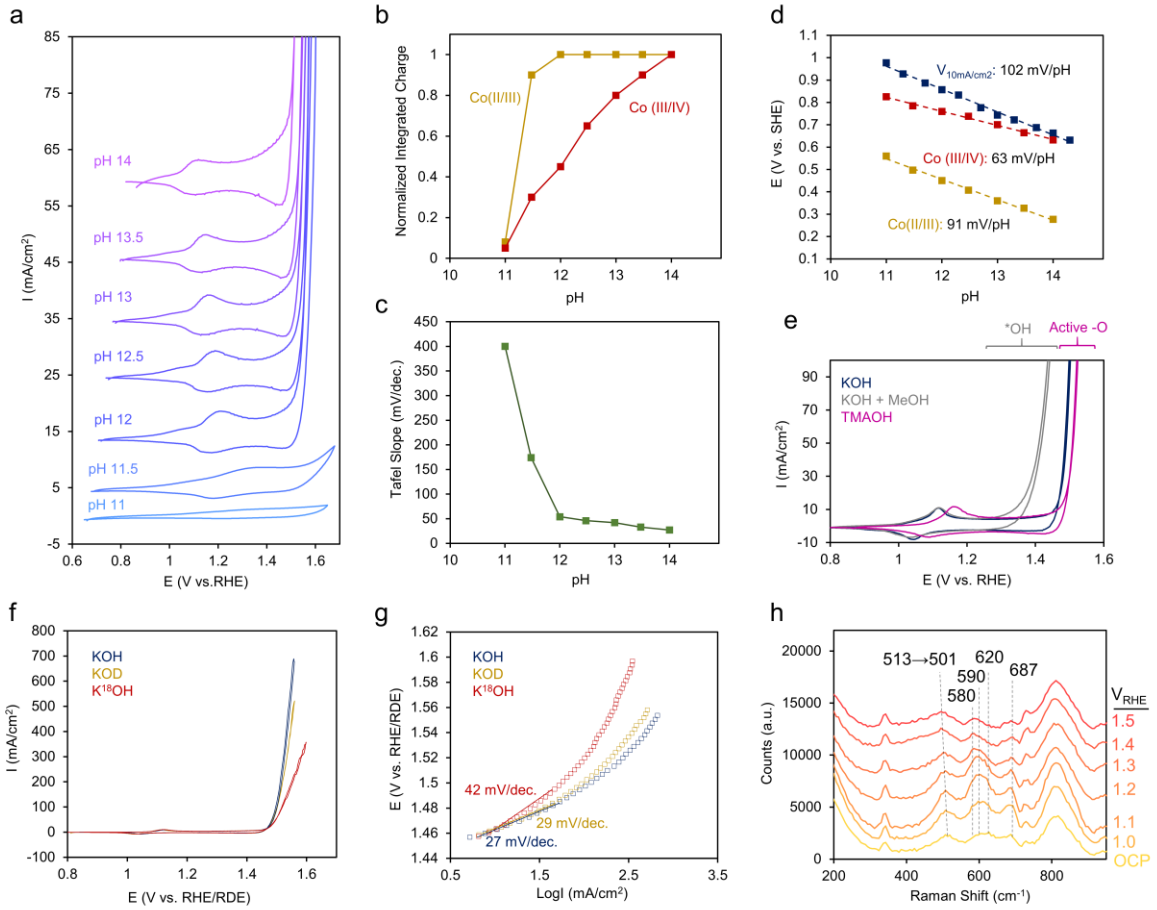
a
I (mA/cm²)
E (V vs.RHE)
pH 14
pH 13.5
pH 13
pH 12.5
pH 12
pH 11.5
pH 11
b
Normalized Integrated Charge
pH
Co(II/III)
Co (III/IV)
c
Tafel Slope (mV/dec.)
pH
d
E (V vs. SHE)
pH
V10mA/cm2: 102 mV/pH
Co (III/IV): 63 mV/pH
Co(II/III): 91 mV/pH
e
I (mA/cm²)
E (V vs. RHE)
*OH
Active -O
KOH
KOH + MeOH
TMAOH
f
I (mA/cm²)
E (V vs. RHE/RDE)
KOH
KOD
K18OH
g
E (V vs. RHE/RDE)
LogI (mA/cm²)
KOH
KOD
K18OH
42 mV/dec.
29 mV/dec.
27 mV/dec.
h
Counts (a.u.)
Raman Shift (cm-1)
513→501
620
590
580
687
VRHE
1.5
1.4
1.3
1.2
1.1
1.0
OCP

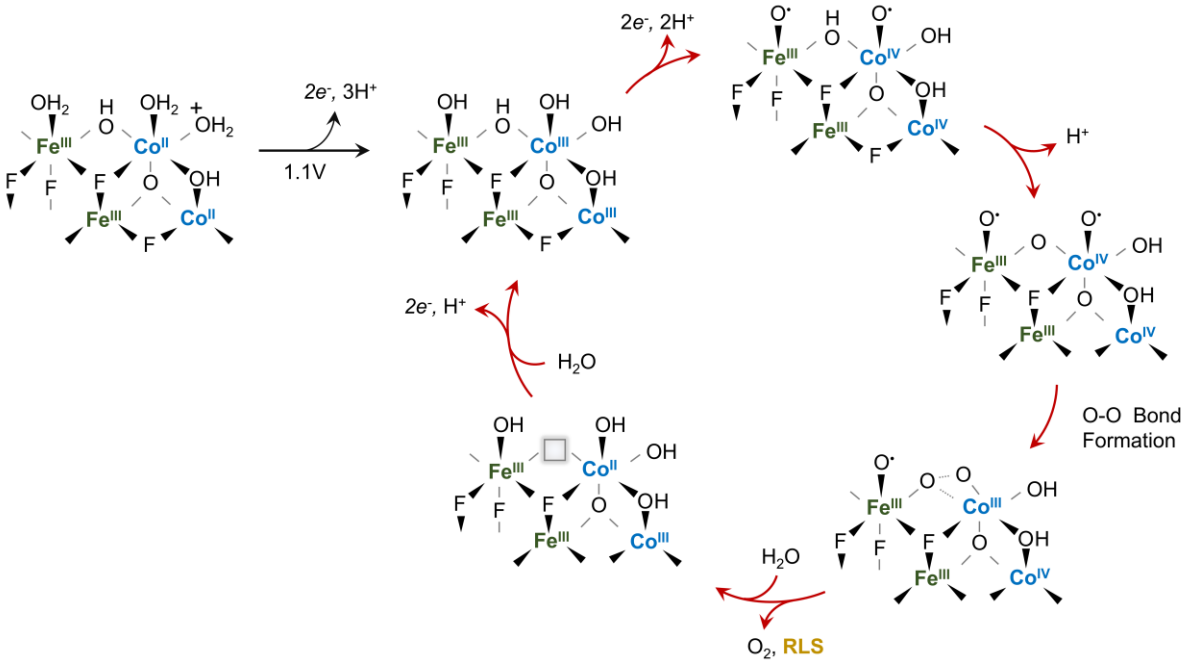
2e-, 3H+
1.1V
2e-, 2H+
H+
O-O Bond
Formation
H2O
O2, RLS
2e-, H+
H2O

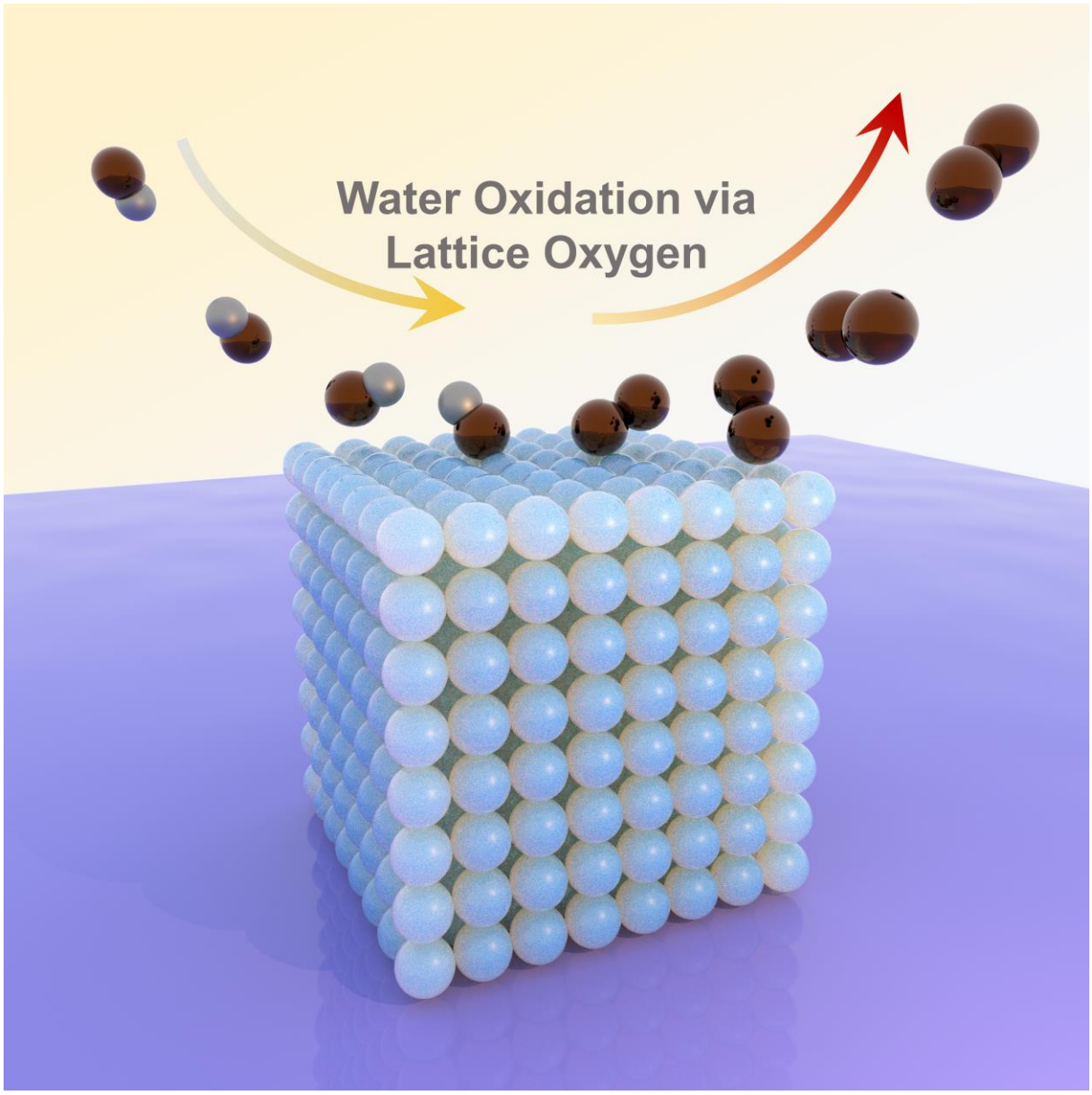

TOC